Article

Templated Synthesis of Cu_2S Hollow Structures for Highly Active Ozone Decomposition

Yishan Jiang , Ying Xu , Qichao Zhang * , Xin Zhao , Feng Xiao * , Xinbo Wang , Guojun Ma *

Posted Date: 16 January 2024

doi: 10.20944/preprints202401.1190.v1

Keywords: Ozone decomposition; Cu_2S; Hollow structured materials; Sacrificial template

Article

Templated Synthesis of Cu_2S Hollow Structures for Highly Active Ozone Decomposition

Yishan Jiang [1], Ying Xu [1], Qichao Zhang [1,*], Xin Zhao [1], Feng Xiao [1,*], Xinbo Wang [1] and Guojun Ma [2,3,*]

[1] Navy Submarine Academy, Qingdao 266199, PR China
[2] State Key Laboratory of Mesoscience and Engineering, Institute of Process Engineering, Chinese Academy of Sciences, Beijing 100190, PR China
[3] School of Chemical Engineering, University of Chinese Academy of Sciences, Beijing, 100049, PR China
* Correspondence: Zhang Qichao, zhangqcocean@163.com; Xiao Feng, qdxuwx@126.com; Ma Guojun, gjma@ipe.ac.cn

Abstract: Nowadays, it is highly desired to develop highly active and humidity-resistive ozone decomposition catalysts to eliminate the ozone contaminant, one of the primary pollutants in the air. In this work, a series of Cu_2S hollow structured materials are rapidly synthesized using different structured Cu_2O templates. The Cu_2S from porous Cu_2O shows the highest ozone catalytic decomposition efficiency of >95% to 400 ppm ozone with a weight hourly space velocity of 480,000 $cm^3g^{-1}h^{-1}$ in dry air. Importantly, the conversion remains>85% in a high relative humidity of 90%. The mechanism is explored by diffusive reflectance infrared spectroscopy, which shows the decomposition intermediate of O_2^{2-}, and the X-ray photoelectron spectroscopy reveals the dual active site of both Cu and S. The EPR and UPS characterization results also explain the superiority of porous Cu_2S catalysts from the material itself. All these results show the effective decomposition of ozone by Cu_2S, especially in harsh environments, promising for active ozone elimination.

Keywords: Cu_2S hollow structure; Cu_2O template; ozone decomposition; DRIFT; high efficiency

1. Introduction

Among the various atmospheric pollutants that humans face today, near-surface ozone (O_3) pollution is a relatively challenging problem[1]. It usually occurs in big cities and is highly associated with precursors of volatile organic compounds (VOCs) and nitrogen oxides (NOx), posing significant challenges to human health[2,3]. O_3 is currently considered the second most harmful air pollutant and is the primary air pollutant in most urban areas during the summer. Correspondingly, there is a widespread and urgent demand for O_3 treatment technology both outdoors and in enclosed spaces. The most efficient ozone treatment technology currently uses precious metal catalysts such as Au and Pd, which have excellent performance but lack economic efficiency[4,5]. Instead, transition metal oxides such as MnOx and Cu_2O are more favorable for high efficiency and low cost O_3 decomposition [6-8].

It should be noted that transition metal oxides are usually highly active in O_3 decomposition in dry air but suffers from water vapor competitive adsorption with O_3 leading to lower activity. In the meanwhile, O_3 pollution is often accompanied by more acidic gas pollutants such as SO_2 and NO_2. For example, Ma et al. [9] shows that though the SO_2 and NO_2 pollution in China's atmosphere has been significantly reduced in recent years, their total amount is still higher than O_3. Mukta et al. [10] reports that the concentration of NO_2 is always higher than O_3 in Gazipur in Bangladesh. The study by Stevens et al. [11] also supports the considerable amount of acidic gases such as NO_2 and SO_2 in the atmosphere of Europe and North America. Therefore, besides humidity interfering, metal oxide catalyst is also prone to combine with acidic substances, which would accelerate the deactivation of the catalysts.

 doi:10.20944/preprints202401.1190.v1

Copper sulfide (Cu_2S), as a narrow bandgap p-type semiconductor, has been widely studied and applied in cutting-edge fields such as photocatalysis and high-temperature superconductivity due to its unique crystal structure and band gap[12-16]. Importantly, Cu_2S exhibits excellent acid resistance because of its extremely low solubility ($K_{sp} = 2\times10^{-47}$)[17,18]. Insolubility brings additional advantages to sulfides in constructing complex morphologies, which are required by catalysts, especially some hollow and microstructures. Chun-Hong Kuo et al. [19] reported that Cu_2O nanoparticles can be gradually transformed into Cu_2S by 0.2 M Na_2S solution in 360 seconds. After being transformed into Cu_2S, the nanoparticles form a hollow cage structure based on their original cubic morphology. For example, Lei Ran et al. [20] reported a synthesis process of double-walled heterostructured $Cu_{2-x}Se/Cu_7S_4$ nano boxes used as a material for quantum dot sensitized solar cells. The complex morphology of this catalyst was synthesized using a simple Cu_2O template. Although the application of Cu_2S materials in CO2 conversion and solar cell materials has attracted increasing attention from researchers, there are currently no reports on the application of CuxS in O_3 decomposition. In the previous study, p-type semiconductor showed relatively higher O_3 decomposition activity than the n-type counterparts [21]. As a typical p-type semiconductor, the performance of Cu_2S in ozone catalytic decomposition is worth exploring, because its convenient morphology construction and stable composition are rare advantages.

Here, Cu_2S hollow structures have been prepared by Cu_2O template routine and are used as ozone decomposition catalyst, which shows high activity and high resistance to relative humidity, promising for the O_3 decomposition in the atmosphere.

2. Experimental

2.1. Synthesis of catalysts

Cu_2S catalyst was prepared using the sacrificial template method. Referring to the synthesis principle in the literature[22-24], three types of Cu_2O templates were synthesized using different methods: cubic, porous, and spherical. The specific methods are as follows.

Cubic Cu_2O: 80 mmol (20 g) $CuSO_4{\cdot}5H_2O$ was dissolved in 250 mL distilled water. Then, 100 mL NaOH solution (4 mol/L) was added dropwise. After further stirring the blue suspension for 30 minutes, 112 mL ascorbic acid (AA) aqueous solution (1 mol/L) was added dropwise within approximately 5 minutes. The solution was then stirred until the suspension gradually turned orange red. The precipitate was separated by centrifugation, washed three times with water and ethanol, and then dried in an 80 °C oven for 8 hours.

Spherical Cu_2O: 20 mmol (3.98g) $Cu(OAC)_2{\cdot}H_2O$ was dissolved in 150 mL distilled water. After completely dissolved, 10 mL NaOH solution (4 mo1/L) was added and stirred for 30 minutes. Then, 20 mL AA aqueous solution (1 mol/L) was added dropwise. The precipitate was obtained by centrifuge, washed three times with water and ethanol, and then dried in an 80 °C oven for 8 hours.

Porous Cu_2O: 20 mmol (5g) $CuSO_4{\cdot}5H_2O$ was dissolved in 150 mL distilled water. After completely dissolved, 10 mL NaOH solution (4 mol/L) was added. After further stirring the blue suspension for 30 minutes, 3.5 g AA powder was added directly. After stirring for 5 minutes, the sediment was separated by centrifuge, washed three times with water and ethanol, and then dried in an 80 °C oven for 8 hours.

Cu_2S hollow structures were synthesized by vulcanizing the three Cu_2O templates. They were added into to a Na_2S aqueous solution in concentration of 2M with a S:Cu molar ratio of 1:2. The suspension was stirred for 15 minutes to react, and then the powders was obtained by separation, washing and drying.

2.2. Characterization of the catalyst

The catalyst's crystal structure was analyzed using an X-ray diffractometer (XRD, X'pert Pro System) manufactured by Panalytical, Netherlands, operating at 40 kV and 40 mA, with Cu Kα radiation (wavelength of 0.154 nm). The scanning range was 5–90° at a speed of 10° min^{-1}. The obtained results were converted to xrdml format using PowDll software, and then imported into

 doi:10.20944/preprints202401.1190.v1

XpertHighscore software for analysis and compared with standard cards in the database. Microscopy analysis was conducted using the ultra-high resolution field emission scanning electron microscope (FESEM, JSM-7800, JEOL, Tokyo, Japan). Fix the Cu_2O/Cu_2S onto the sample stage using conductive tape and capture the sample morphology under an accelerated voltage of 15 kV after spray-gold treatment. Adjust the focus and brightness, then record the image at a magnification of 50,000 to 100,000. The transmission electron microscope photos (TEM) and High-resolution transmission electron microscopy (HRTEM) were conducted using a JEOL JEM-2100F transmission electron microscope (JEOL, Aichi, Japan) at an accelerating voltage of 200 kV. The catalyst samples were dispersed in ethanol and loaded onto copper grids covered with microgrid carbon films. The Cu_2S products' specific surface areas were analyzed using the Brunauer–Emmett–Teller (BET) method with a Surface Area Analyzer Micromeritics (ASAP2460, USA) at a temperature of liquid nitrogen (−196 °C) with N_2 gas as the adsorbate. Prior to the analysis, the samples were dried at 120 °C for 4 hours and then degassed at 150 °C for 1 hour. The pore size distributions were determined from the desorption branches of the isotherms based on the Barrett–Joyner–Halenda (BJH) theory. Surface chemical bonds and chemical states of the catalysts were characterized by X-ray photoelectron spectroscopy (XPS, ESCALAB 250XI, Thermo Fisher, Waltham, Massachusetts, USA) using a monochromatic Al Kα X-ray source (1486 eV) with a beam size of 200 μm. Charge compensation was achieved by dual-beam charge neutralization, and the binding energy was corrected by setting the binding energy of the hydrocarbon C 1s feature to 284.8 eV. The electron paramagnetic resonance (EPR) signals of radicals' spin trapped were carried out on a Bruker EMXplus-6/1 (Munich, Germany) spectrometer by spin-trap reagents of DMPO and TEMP for S vacancy. The ultraviolet photoelectron spectroscopy (UPS) testing instrument is the ESCALab 250Xi multi energy electron spectrometer produced by ThermoScientific (Massachusetts, USA). During UPS testing, a He I ultraviolet light source (h ≈ 21.22 eV) was selected, and the vacuum in the analysis room was about 3 × 10^{-6} Pa. The bias voltage was set at -5 eV in the experiment. An appropriate energy analyzer was selected for energy and spectral scanning range, and the corresponding secondary electron energy distribution curve was recorded. The measurement of the secondary electron cutoff edge (E_{cutoff}) and Fermi edge (E_{Fermi}) involves cleaning the surface of the semiconductor sample with an Ar^+ beam and correcting it with an Au standard sample before testing. Raman spectroscopy was analyzed at LabRAM HR Evolution (Horiba, Kyoto, Japan). The measurement span is from 1500 to 200 cm^{-1} at room temperature. The 633 nm line of the laser was used as the excitation source, with the capability of supplying 250 mW. Intermediate products and surface adsorption groups on Cu_2S catalyst is characterized via FTIR-DRIFTS (Diffuse Reflectance Infrared Fourier Transform Spectroscopy), the infrared spectrometer is made by BRUKER (INVENIO, Ettlingen, Germany). The sample was mixed with equal mass KBr powder in an in-situ cell, and measured wavelength range is from 400 to 4000 cm^{-1}. After the sample is placed in the gas cell, the entire experimental section is heated to 150 °C under nitrogen protection for 2 hours, and then cooled to room temperature to drive away moisture and other adsorbed gases. Before testing, the sample is first purged with dry nitrogen gas for 1 hour, followed by oxygen as the background. Afterwards, activate the ultraviolet ozone generation device in the oxygen gas path, and the ozone concentration can be maintained at approximately 30-50ppm at a flow rate of 100sccm. Stopping the introduction of ozone refers to shutting down the ozone generator and continuing to blow the sample with the original flow rate of O_2/N_2 gas.

2.3. Ozone decomposition test

The O_3 decomposition performance was tested in a U-shape quartz tube reactor (diameter 5.5 mm) at 25 °C with 50 mg (40–60 mesh) Cu_2S mixed with 450 mg quartz sand. The overall weight hourly space velocity (WHSV) remained at 480,000 $cm^3\ g^{-1}{\cdot}h^{-1}$. Ozone was generated at concentrations from 200 to 400 ppm by a commercial ozone generator (COM-AD-01-OEM, ANSEROS COMPANY, Anshan, China), and the inlet and outlet ozone concentrations were analyzed by an ozone monitor (model 106MH, 2B Technologies, USA). The ozone conversion was calculated as: 100% × (O_3 inlet - O_3 outlet) / O_3 inlet. The moisture was produced by bubbling water with the airflow, in the bubbling

 doi:10.20944/preprints202401.1190.v1

device, it can be ensured that the relative humidity is greater than 90. The relative humidity (RH) was measured by a humidity and temperature sensor meter (center 310 RS-232, TES, China).

3. Results and discussion

Cu_2S was synthesized using Cu_2O with porous, spherical, and cubic morphologies as sacrificial templates, which are named Cu_2S porous (Cu_2S-P), Cu_2S sphere (Cu_2S-S) and Cu_2S cube (Cu_2S-C). The O_3 decomposition performance of Cu_2S varies significantly among the three morphologies, with Cu_2S-P exhibiting substantially better performance (**Figure 1a**). More than 95% of 400 ppm O_3 can be decomposed at a space velocity of WHSV 480,000 $cm^3\ g^{-1}{\cdot}h^{-1}$ in dry conditions. To verify whether Cu_2S is a catalyst or a simple chemically absorbing agent for O_3, a durability test was conducted on Cu_2S-P in **Figure 1b**. After working continuously for 18 hours, the cumulative amount of O_3 processed was 3.86 mmol, which was tens of times higher than the amount of Cu_2S-P substance (50 mg, ~0.31 mmol). After dealing with much more O_3 than itself, the O_3 decomposition activity still exceeds 90%, which proves the catalytic process of ozone decomposition by Cu_2S, rather than a simple oxidation/reduction process of Cu_2S and O_3. At the same time, the catalytic decomposition performance of Cu_2S in high-humidity environments was investigated. As shown in **Figure 1c**, due to the competitive adsorption of water molecules, high humidity has a particular impact on its catalytic performance. However, the conversion still maintains over 85% performance under conditions of 480,000 $cm^3g^{-1}\ h^{-1}$ and humidity greater than 90%, showing the good humidity resistance of this catalyst.

To investigate the relationship between structure and performance further, XRD characterization was performed on three types of Cu_2S. In **Figure 2**, the characteristic peak intensity in Cu_2S-P and Cu_2S-S is relatively weak, with most Cu_2S exhibiting an amorphous structure. Cu_2S-C particles crystallize better, and the three types of Cu_2S conform with the *calcite alpha low* in the standard card (JCPDS Ref. code 00-009-0328). High crystallinity means fewer defects, which is usually detrimental to the performance of heterogeneous catalysts, which may be the reason for the poor performance of Cu_2S-C.

To further understand the specific morphologies of Cu_2S samples and their templates, FESEM and TEM techniques were used as shown in **Figure 3**. Through SEM images, all three Cu_2O templates exhibit different morphologies: the sphere template has fine particles on the surface (**Figure 3a**), the cube template reveals varying sizes (**Figure 3b**), and the porous templates are formed by the accumulation of many small particles (**Figure 3c**). Due to the much lower solubility product of Cu_2S in water compared to Cu_2O[19], Cu_2O dispersed in water is prone to generate more insoluble Cu_2S with S^{2-}, and the morphology of the developed product is correlated with the sacrificial template (Cu_2O). However, due to differences in mass transfer rates, internal substances quickly transfer to the surface through mass transfer channels and form voids inside, as **Figure 3d** and **e**, which is described in the literature as the Kirkendall effect [25,26]. However, the tiny particles in **Figure 3f** were not observed to have apparent hollow structures, and it is speculated that the nanoscale effect of the stacked small particles is enhanced, thereby overcoming the interface resistance and fusing. All these processes can be clearly shown in the schematic view in **Figure 4**: Taking spherical Cu_2O particles as an example, when spherical particles are suspended in water solution, the ions (Cu^+) in the solution are attracted by the surface charge of the particles, forming an electrical double layer. This electrical double layer leads to an increase in the solution concentration near the particle surface, creating a concentration gradient in the solution. Due to the concentration gradient generating osmotic pressure, solvent molecules accumulate near the particle surface, further increasing the solution concentration near the particle surface. The particle core transports Cu to the surface through several mass transfer channels, gradually forming voids inside. This process represents the Kirkendall effect in spherical particles. This effect is equally applicable in both cubic and porous structures.

Preprints (www.preprints.org) | NOT PEER-REVIEWED | Posted: 16 January 2024 doi:10.20944/preprints202401.1190.v1

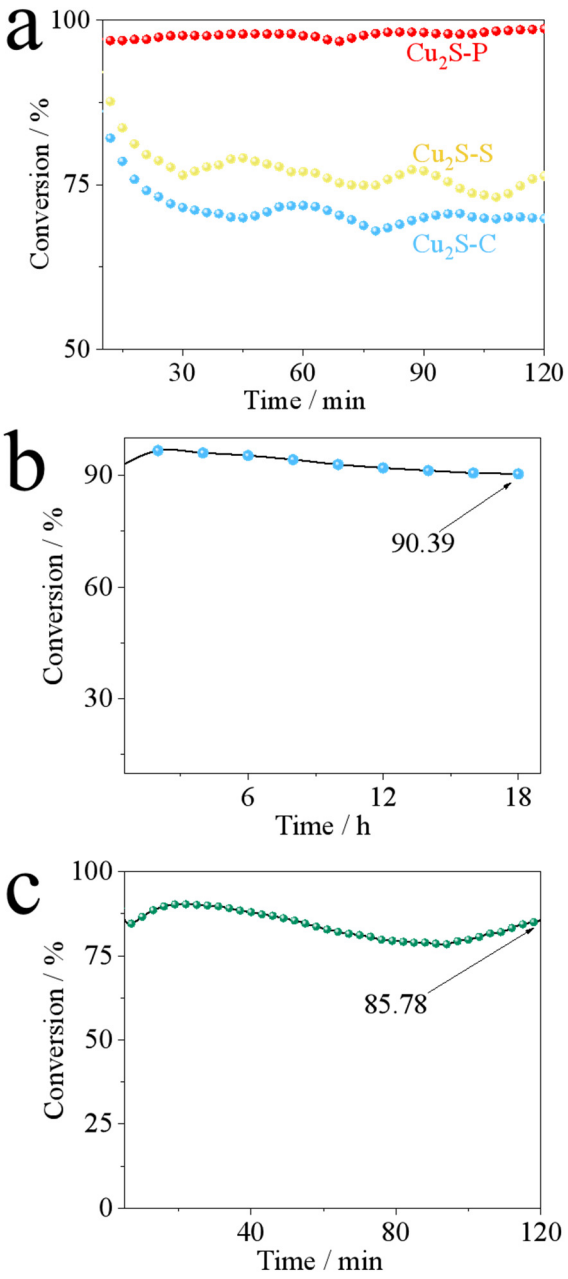

Figure 1. Cu_2S catalytic performance testing. (a) Cu_2S with different morphologies for ozone decomposition at room temperature, 480,000 $cm^3\ g^{-1}{\cdot}h^{-1}$ (50 mg catalyst, 400 sccm airflow), 400 ppm dry O_3, (b) durability testing of CuS-P at room temperature, 480,000 $cm^3\ g^{-1}{\cdot}L^{-1}$ (50 mg catalyst, 400 sccm), 200 ppm dry O_3, (c) performance of Cu_2S-P on catalytic decomposition of 200 ppm O_3 at 480,000 $cm^3\ g^{-1}{\cdot}h^{-1}$ and high humidity (>90% RH).

Another important property of the catalyst is the specific surface area and surface pore structure. The characterization results of three types of Cu_2S are shown in **Table 1**. According to the BET characterization results, Cu_2S-P has the largest specific surface area and the smallest average pore size of about 5 nm. Although studies [24,27] have shown that specific surface area is not a decisive indicator of the performance of ozone catalysts, Cu_2S-P has a larger specific surface area and pore capacity compared to other structures, which can improve its contact efficiency with ozone gas flow and is a favorable factor in situations where surface chemical properties are similar.

Preprints (www.preprints.org) | NOT PEER-REVIEWED | Posted: 16 January 2024 doi:10.20944/preprints202401.1190.v1

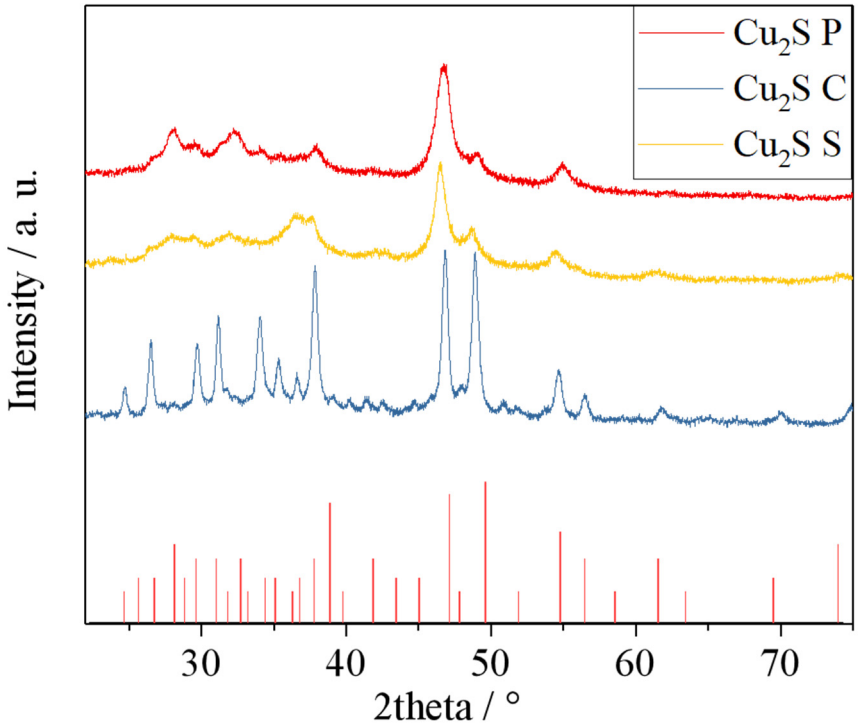

Figure 2. XRD patterns of Cu_2S samples.

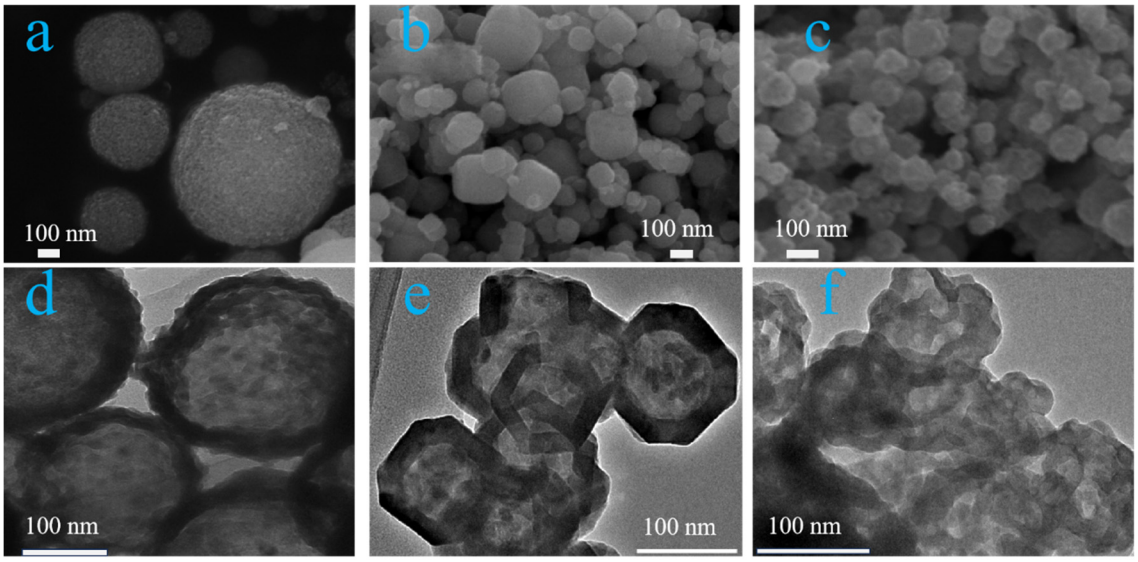

Figure 3. SEM and TEM image of the Cu_2S and template. (a) SEM of Cu_2O sphere template, (b) SEM of Cu_2O cube template, (c) SEM of Cu_2O cube template, (d) TEM image of Cu_2S-S, (e) TEM image of Cu_2S-C, and (f) TEM image of Cu_2S-P.

Table 1. Specific surface area and pore structure parameters of Cu_2S.

Sample	BET Surface Area (m^2/g)	Pore Size (Å)	Pore Volume (cm^3/g)
Cu_2S-C	11.48	71.31	0.02047
Cu_2S-S	7.31	111.75	0.02043
Cu_2S-P	14.67	59.25	0.02174

Preprints (www.preprints.org) | NOT PEER-REVIEWED | Posted: 16 January 2024 doi:10.20944/preprints202401.1190.v1

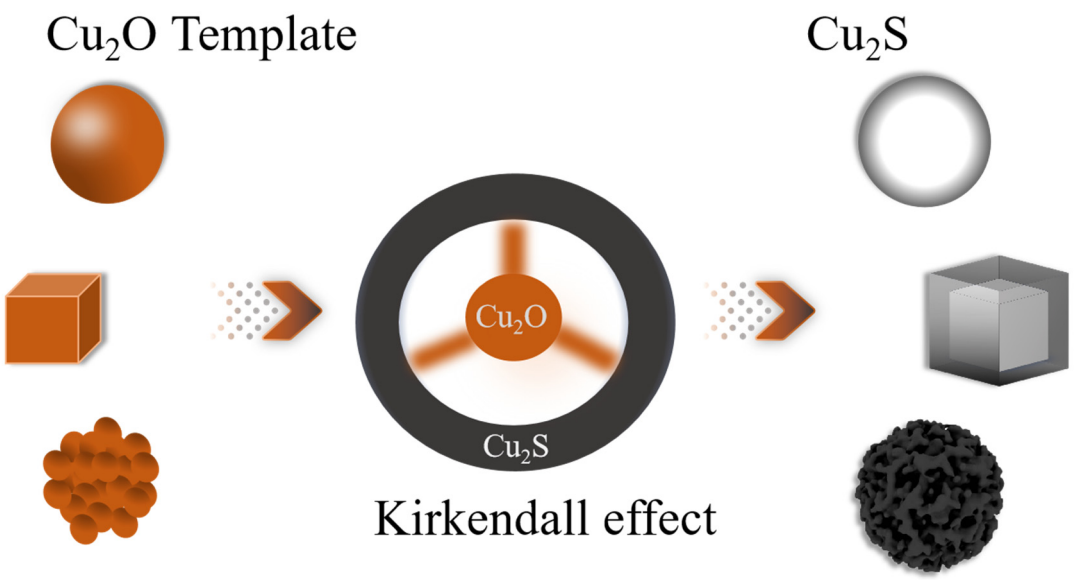

Figure 4. Schematic diagram of structural evolution process, the internal Cu_2O is rapidly transferred to the surface through several mass transfer channels, forming Cu_2S hollow structures.

Although the sample with the best performance also has the largest specific surface area, overall, the difference in specific surface area among the three morphologies of Cu_2S particles is not significant. This seems difficult to explain the significant performance differences, especially in Cu_2S-P. Therefore, EPR characterization was employed to measure the sulfur vacancies in three different morphologies of Cu_2S. **Figure 5** shows that Cu_2S-P has prominent sulfur vacancies[28], which are not present in other samples. This can be attributed to the generation of S vacancies caused by the nanoscale effect of small particles during mass transfer. More sulfur vacancies mean more defects and crystal structure imbalances, which are usually beneficial for catalytic reactions. It is generally believed in the literature that these sulfur vacancies are active sites [29,30].

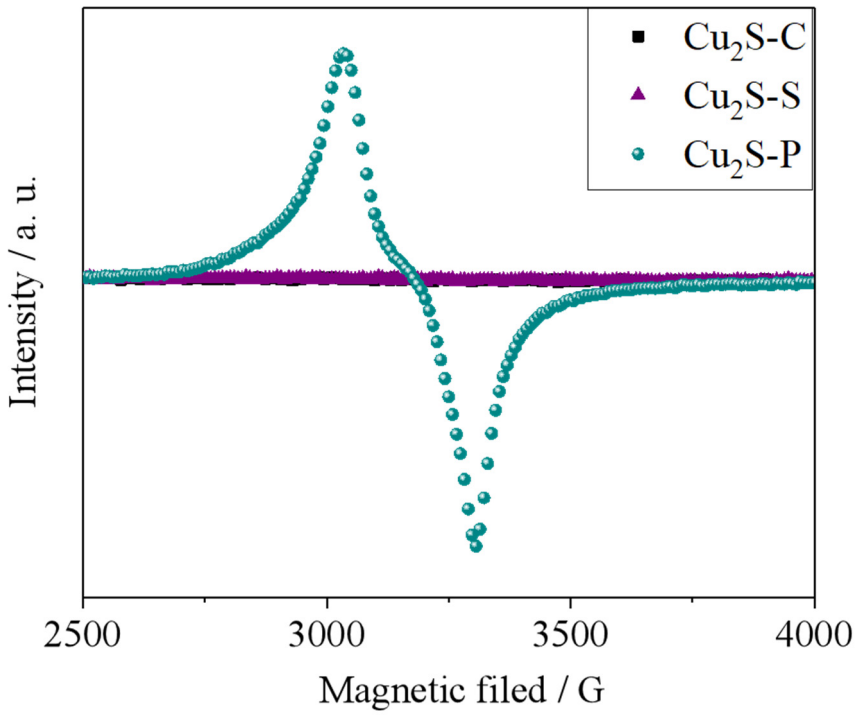

Figure 5. EPR signal of S vacancies in different samples.

Preprints (www.preprints.org) | NOT PEER-REVIEWED | Posted: 16 January 2024 doi:10.20944/preprints202401.1190.v1

The work function (Φ) has an important impact on the performance of semiconductor catalysts, which can affect their electron transfer, reaction activity, and photocatalytic performance, thereby affecting the efficiency and effectiveness of catalysts in catalytic reactions[31]. The photoelectron spectroscopy method obtains the escape work of materials by measuring the non-elastic secondary electron cutoff edge. According to the basic energy relationship of photoelectric emission, the energy interval from the cutoff edge of inelastic scattering secondary electrons to the vacuum level is the energy of photons[32]. Therefore, the work function is calculated as follows:

$$\Phi = h\nu - (E_{Fermi} - E_{cutoff})$$

Figure 6 shows that there are significant differences in the work functions of the three morphologies of Cu_2S materials. Although the work function is usually not significantly correlated with the catalytic performance of the material, the lower work function of Cu_2S-P (3.04eV) material means that electrons have higher transfer efficiency in the system, which is more favorable for the adsorption and desorption of ozone molecules. This also explains that Cu_2S-S has a lower specific surface area and similar pore capacity, while its catalytic performance is not inferior to Cu_2S-C. Although we have explained in the discussion of the data results in **Table 1** that the internal surface areas of hollow spheres and hollow cubes may be difficult to participate in catalytic reactions, there is no difference in the adsorption desorption data of mesoporous performance, and the difference in their work functions may be one of the determining factors.

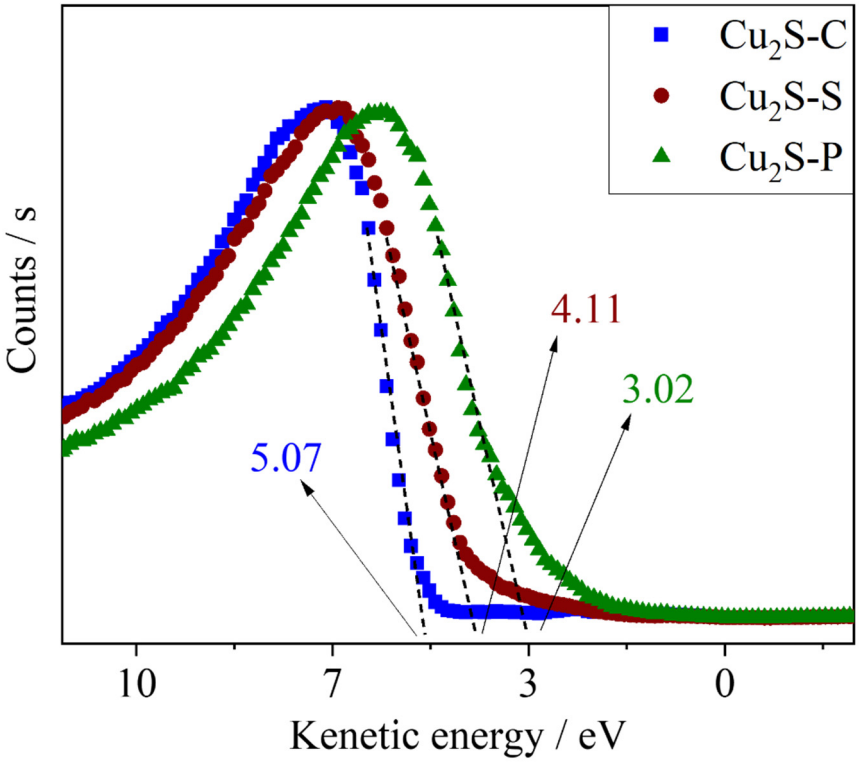

Figure 6. UV photoelectron spectroscopy of samples with different morphologies. The instrument has automatically calibrated the Fermi edge, and then corrected the abscissa using the emitted photon kinetic energy and bias voltage. The intercept can be equivalent to the work function (Φ).

To reveal the process of ozone conversion on the catalyst surface, in situ FTIR spectroscopy was employed to detect changes in surface functional groups after exposure to ozone. In **Figure 7a**, the introduction of ozone produced a weak O_2^{2-}[33] peak at a wavenumber of 756 cm^{-1}, and in **Figure 7b**, the peak weakens after stopping the ozone for a period, which is similar to the transition metal oxides in the literature[34,35], which can be attributed to the classical reaction process of ozone on sulfide surfaces. Due to the widespread presence of ppm-level water vapor in gas cylinders, its

Preprints (www.preprints.org) | NOT PEER-REVIEWED | Posted: 16 January 2024 doi:10.20944/preprints202401.1190.v1

characteristic peaks gradually increase over time. In addition, signals generated by S–O (1060 cm^{-1}) and S=O (1350-1420 cm^{-1}) stretching vibrations[36] were observed on the surface of Cu_2S and did not disappear after the introduction of ozone was stopped. This indicates that during the surface transformation process of ozone, a layer of sulfate salt is formed on the surface of Cu_2S. The literature indicates that a surface sulfate layer helps maintain the stability of catalyst particles[37]. This result is consistent with **Figure 5**. The S vacancy on the surface is beneficial for O_3 adsorption, and the adsorbed O atom fills the vacancy, stabilizing the surface chemical structure and facilitating further participation in surface reactions.

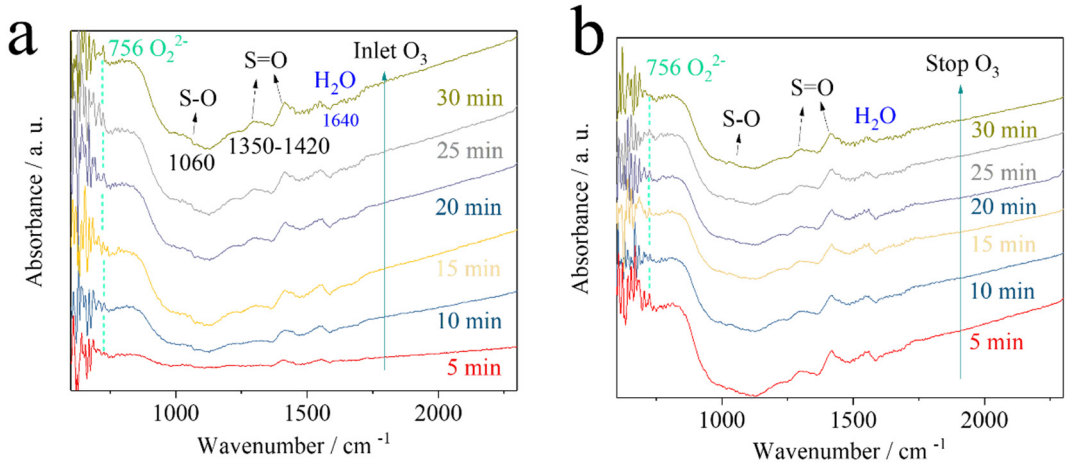

Figure 7. In situ FTIR spectroscopy characterization of Cu_2S in (a) O_2/ozone mixed inlet and (b) stopped ozone airflow.

XPS characterization was performed on Cu_2S-P before and after the reaction to study the mechanism of the catalytic decomposition of ozone. In **Figure 8a,** the S 2p 1/2 and S 2p 2/3 peaks at ~162 eV can be attributed to the S – Cu bond [38], and peaks at ~169 eV can be attributed to the S – O bond [39]. After continuous operation for 18 hours, the S – O bond in Cu_2S-P was enhanced, and the Cu II peak was clearly observed in the shoulder peak of the dominant Cu I peak (**Figure 8b)**. The enhancement of S – O bonds indicates that the surface S atoms are also effective active sites besides the commonly believed active sites of Cu atoms and defects. Secondly, after 18 hours of continuous catalysis of O_3, there is a certain degree of oxidation on the catalyst surface, but the initial composition is still dominant. This indicates that the durability of sulfide-catalytic materials and oxide-catalyzed ozone is similar. In some previous studies[40], the same situation is commonly observed in metastable transition metal oxides. Since the test sample for XPS is Cu_2S-P, this may also be due to a large number of S vacancies on the surface being filled by O atom, which has a high electronegativity and is prone to further electron valence change in Cu. Combined with the surface depth limitation of XPS testing, this phenomenon is more pronounced on the surface.

In addition, Raman spectroscopy characterization was performed on Cu_2S-P before and after use, and the results are shown in **Figure 9**. According to the literature[41-43], the Raman peaks at 268 cm^{-1} and 472 cm^{-1} are attributed to Cu_2S, while the Raman peak at 284 cm^{-1} is attributed to Cu_2O. Consistent with the XPS characterization results, Raman spectroscopy shows that although there is a weak CuO signal in the catalyst after 18 hours of use, Cu_2S is still the main component, further proving the catalyst's stability.

Preprints (www.preprints.org) | NOT PEER-REVIEWED | Posted: 16 January 2024 doi:10.20944/preprints202401.1190.v1

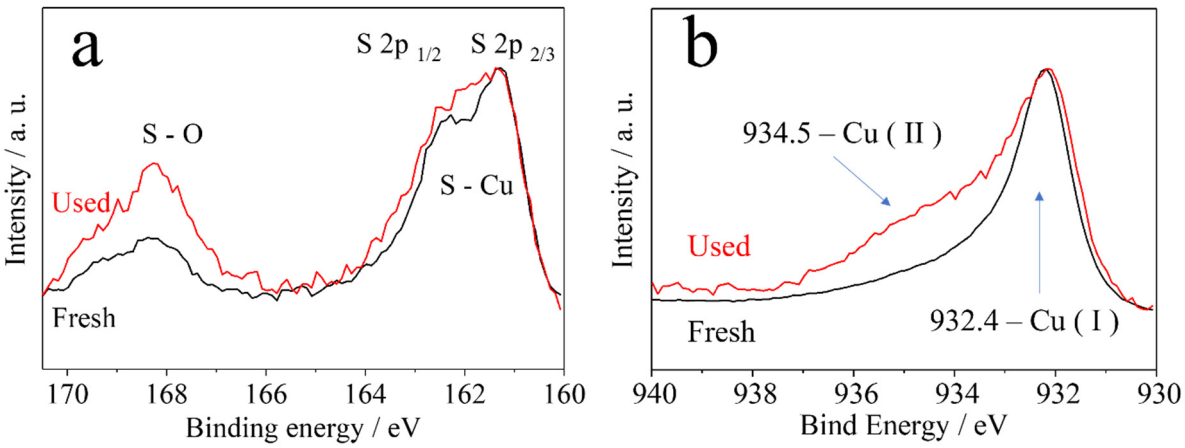

Figure 8. XPS characterization of Cu_2S-P deconvolution peak before and after reaction. (a) S 2p scan and (b) Cu 2p scan.

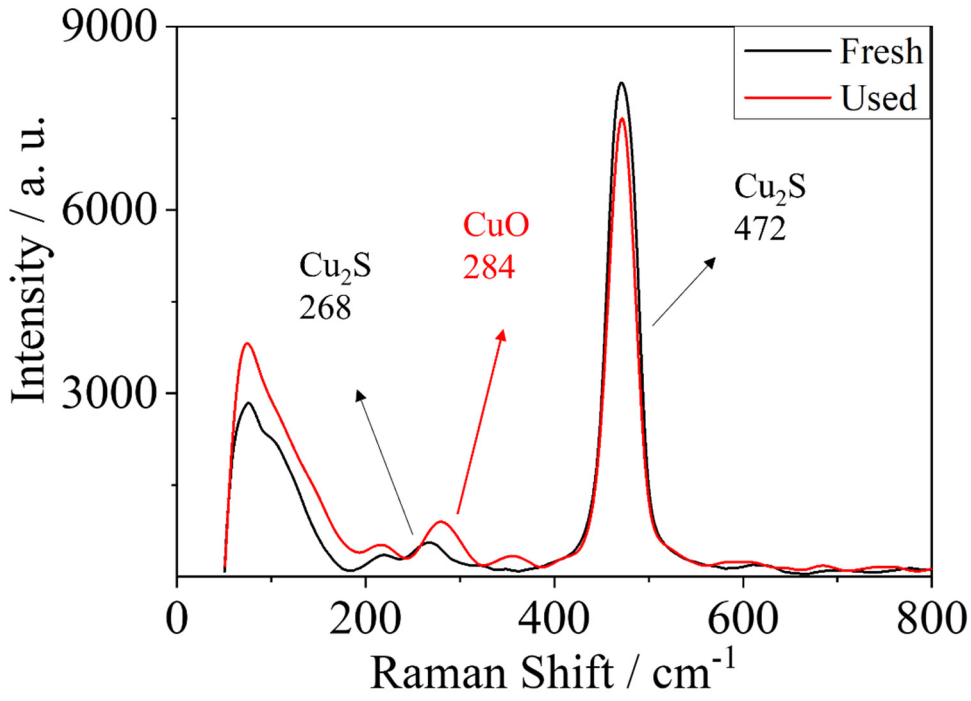

Figure 9. Raman spectra of Cu2S-P, as of and after the ozone decomposition.

Based on the above characterization and test results, it can be inferred that Cu_2S, a p-type semiconductor similar to Cu_2O, has a similar catalytic principle for ozone decomposition. However, the active center has been replaced by metal atoms and oxygen defects in transition metal oxides with metal and surface sulfur atoms. The catalytic process and intermediate products, as proposed by Oyama et al. [21], are described in Equations (1-3).

$$O_3 + \text{active site (Cu, S)}^* \rightarrow O_2 + O^- \quad (1)$$

$$O_3 + O^- + * \rightarrow O_2 + O_2^{2-} \quad (2)$$

$$O_2^{2-} \rightarrow O_2 + 2^* \quad (3)$$

The charged intermediate products in the process of ozone decomposition have strong oxidizing properties, which can quickly oxidize some surfaces and transform them into CuO. This heterostructure is not entirely unfavorable for ozone decomposition, as shown in **Figure 1c**, where

the performance improves in the first few hours and then slightly decreases. This is very consistent with the performance of cuprous oxide catalytic materials, and all these results show the promising prospect of the Cu_2S catalyst for effective ozone decomposition.

4. Conclusions

Using the Kirkendall effect, Cu_2S hollow structured materials with different morphologies were rapidly synthesized from different shaped Cu_2O templates. The catalytic effect of Cu_2S material on the ozone decomposition process has been confirmed by combining actual test results and material characterization before and after the reaction. Its catalytic efficiency of 400 ppm ozone can exceed 95% at WHSV of 480,000 $cm^3g^{-1}\cdot h^{-1}$ under dry conditions, one of the highest in the literature. The DRIFT results show the intermediate O_2^{2-}, showing the catalytic reaction mechanism. And sulfur can be also active in ozone decomposition as illustrated by XPS, which has broadened the application prospects in the catalytic decomposition of ozone.

Author Contributions: Conceptualization, methodology: Zhang Qichao, Xiao Feng, Ma Guojun; formal analysis, investigation, data curation, writing— original draft preparation: Jiang Yishan, Xu Ying, Zhao Xin; Writing — review and editing, resources, supervision: Xiao Feng and Ma Guojun; software: Wang Xinbo.

Funding: This research was financially supported by research fund of State Key Laboratory of Mesoscience and Engineering (MESO-23-A06).

Data Availability Statement: The data presented in this work are available on request from the corresponding author.

Acknowledgments: Not applicable.

Conflicts of Interest: The authors declare that they have no known competing financial interests or personal relationships that could have appeared to influence the work reported in this paper.

Reference

1. Brunekreef, B.; Holgate, S.T. Air pollution and health. *Lancet* **2002**, *360*, 1233-1242, doi:10.1016/s0140-6736(02)11274-8.
2. Taylan, O.; Alkabaa, A.S.; Alamoudi, M.; Basahel, A.; Balubaid, M.; Andejany, M.; Alidrisi, H. Air Quality Modeling for Sustainable Clean Environment Using ANFIS and Machine Learning Approaches. *Atmosphere* **2021**, *12*, 713.
3. Li, Y.; Yin, S.; Yu, S.; Bai, L.; Wang, X.; Lu, X.; Ma, S. Characteristics of ozone pollution and the sensitivity to precursors during early summer in central plain, China. *Journal of Environmental Sciences* **2021**, *99*, 354-368, doi:https://doi.org/10.1016/j.jes.2020.06.021.
4. Touati, H.; Mehri, A.; Karouia, F.; Richard, F.; Batiot-Dupeyrat, C.; Daniele, S.; Clacens, J.-M. Low-Temperature O3 Decomposition over Pd-TiO2 Hybrid Catalysts. *Catalysts* **2022**, *12*, 448.
5. Z.;, H.; Y.;, L.; Y.;, G.; D., C. Supported gold catalysts used for ozone decomposition and simultaneous elimination of ozone and carbon monoxide at ambient temperature. *Applied Catalysis B: Environmental* **2001**, *33*, 217-222, doi:10.1016/S0926-3373(01)00172-2.
6. Gong, S.; Wu, X.; Zhang, J.; Han, N.; Chen, Y. Facile solution synthesis of Cu_2O–CuO–$Cu(OH)_2$ hierarchical nanostructures for effective catalytic ozone decomposition. *Cryst. Eng. Comm.* **2018**, *20*, 3096-3104, doi:10.1039/C8CE00203G.
7. Deng, H.; Kang, S.; Ma, J.; Wang, L.; Zhang, C.; He, H. Role of Structural Defects in MnOx Promoted by Ag Doping in the Catalytic Combustion of Volatile Organic Compounds and Ambient Decomposition of O3. *Environmental Science & Technology* **2019**, *53*, 10871-10879, doi:10.1021/acs.est.9b01822.
8. Wang, A.; Zhang, L.; Guan, J.; Wang, X.; Ma, G.; Fan, G.; Wang, H.; Han, N.; Chen, Y. Highly efficient ozone elimination by metal doped ultra-fine Cu2O nanoparticles. *Journal of Environmental Sciences* **2022**, doi:https://doi.org/10.1016/j.jes.2022.06.008.
9. Chu, B.; Ma, Q.; Liu, J.; Ma, J.; Zhang, P.; Chen, T.; Feng, Q.; Wang, C.; Yang, N.; Ma, H.; et al. Air Pollutant Correlations in China: Secondary Air Pollutant Responses to NOx and SO2 Control. *Environmental Science & Technology Letters* **2020**, *7*, 695-700, doi:10.1021/acs.estlett.0c00403.

10. Mukta, T.A.; Hoque, M.M.M.; Sarker, M.E.; Hossain, M.N.; Biswas, G.K. Seasonal variations of gaseous air pollutants (SO2, NO2, O3, CO) and particulates (PM2.5, PM10) in Gazipur: an industrial city in Bangladesh. *Advances in Environmental Technology* **2020**, *6*, 195-209, doi:10.22104/aet.2021.4890.1320.
11. Stevens, C.J.; Bell, J.N.B.; Brimblecombe, P.; Clark, C.M.; Dise, N.B.; Fowler, D.; Lovett, G.M.; Wolseley, P.A. The impact of air pollution on terrestrial managed and natural vegetation. *Philosophical Transactions of the Royal Society A: Mathematical, Physical and Engineering Sciences* **2020**, *378*, 20190317, doi:doi:10.1098/rsta.2019.0317.
12. Ranjith, K.S.; Ranjith Kumar, D.; Huh, Y.S.; Han, Y.-K.; Uyar, T.; Rajendra Kumar, R.T. Promotional Effect of Cu2S–ZnS Nanograins as a Shell Layer on ZnO Nanorod Arrays for Boosting Visible Light Photocatalytic H2 Evolution. *The Journal of Physical Chemistry C* **2020**, *124*, 3610-3620, doi:10.1021/acs.jpcc.9b09666.
13. Ansari, M.Z.; Faraz, M.; Munjal, S.; Kumar, V.; Khare, N. Highly dispersible and uniform size Cu2ZnSnS4 nanoparticles for photocatalytic application. *Advanced Powder Technology* **2017**, *28*, 2402-2409, doi:https://doi.org/10.1016/j.apt.2017.06.023.
14. Wang, S.; Huang, Q.; Wen, X.; Li, X.-y.; Yang, S. Thermal oxidation of Cu2S nanowires: A template method for the fabrication of mesoscopic CuxO (x = 1,2) wires. *Physical Chemistry Chemical Physics* **2002**, *4*, 3425-3429, doi:10.1039/B201561G.
15. Zhu, S.; Wu, W.; Li, Z.; Luo, J. First-order transition in LK-99 containing Cu2S. *Matter* **2023**, doi:https://doi.org/10.1016/j.matt.2023.11.001.
16. Ahmed, H.S.; Mohammed, R.Y. The Effect of Deposition Parameters on Morphological and Optical Properties of Cu2S Thin Films Grown by Chemical Bath Deposition Technique. *Photonics* **2022**, *9*, 161.
17. Chen, T.-W.; Rajaji, U.; Chen, S.-M.; Govindasamy, M.; Paul Selvin, S.S.; Manavalan, S.; Arumugam, R. Sonochemical synthesis of graphene oxide sheets supported Cu2S nanodots for high sensitive electrochemical determination of caffeic acid in red wine and soft drinks. *Composites Part B: Engineering* **2019**, *158*, 419-427, doi:https://doi.org/10.1016/j.compositesb.2018.09.099.
18. Honarnezhad, R.; Fathinia, M.; Khataee, A. Mechanical production and sonocatalytic application of Cu2S nanoparticles for degradation of isopropylxanthic acid: Kinetic modeling via white and black box methods. *Journal of Molecular Liquids* **2019**, *287*, 110899, doi:https://doi.org/10.1016/j.molliq.2019.110899.
19. Kuo, C.-H.; Chu, Y.-T.; Song, Y.-F.; Huang, M.H. Cu2O Nanocrystal-Templated Growth of Cu2S Nanocages with Encapsulated Au Nanoparticles and In-Situ Transmission X-ray Microscopy Study. *Advanced Functional Materials* **2011**, *21*, 792-797, doi:https://doi.org/10.1002/adfm.201002108.
20. Ran, L.; Yin, L. Double-walled heterostructured Cu2−xSe/Cu7S4 nanoboxes with enhanced electrocatalytic activity for quantum dot sensitized solar cells. *CrystEngComm* **2017**, *19*, 5640-5652, doi:10.1039/C7CE01112A.
21. Dhandapani, B.; Oyama, S.T. Gas phase ozone decomposition catalysts. *Applied Catalysis B-Environmental* **1997**, *11*, 129-166, doi:10.1016/s0926-3373(96)00044-6.
22. Liu, J.; Gao, Z.; Han, H.; Wu, D.; Xu, F.; Wang, H.; Jiang, K. Mesoporous Cu2O submicro-spheres, facile synthesis and the selective adsorption properties. *Chemical Engineering Journal* **2012**, *185-186*, 151-159, doi:https://doi.org/10.1016/j.cej.2012.01.064.
23. Zhang, Y.; Wang, D.; Zhang, X.; Qu, F. Template-Free Synthesis of Porous Cu₂O Nanospheres at Room Temperature and Investigation on Their Adsorption Property. *Journal of Nanomaterials* **2013**, *2013*, 378919, doi:10.1155/2013/378919.
24. Gong, S.; Wang, A.; Zhang, J.; Guan, J.; Han, N.; Chen, Y. Gram-scale synthesis of ultra-fine Cu2O for highly efficient ozone decomposition. *RSC Advances* **2020**, *10*, 5212-5219, doi:10.1039/C9RA09873A.
25. Minguez-Bacho, I.; Courté, M.; Fan, H.J.; Fichou, D. Conformal Cu₂S-coated Cu₂O nanostructures grown by ion exchange reaction and their photoelectrochemical properties. *Nanotechnology* **2015**, *26*, 185401, doi:10.1088/0957-4484/26/18/185401.
26. Gusak, A.M.; Tu, K.N. Interaction between the Kirkendall effect and the inverse Kirkendall effect in nanoscale particles. *Acta Materialia* **2009**, *57*, 3367-3373, doi:https://doi.org/10.1016/j.actamat.2009.03.043.
27. Gong, S.Y.; Chen, J.Y.; Wu, X.F.; Han, N.; Chen, Y.F. In-situ synthesis of Cu_2O/reduced graphene oxide composite as effective catalyst for ozone decomposition. *Catalysis Communications* **2018**, *106*, 25-29, doi:10.1016/j.catcom.2017.12.003.
28. Zhang, H.; Deng, L.; Chen, J. How $M0S_2$ assisted sulfur vacancies featured Cu_2S in hollow Cu_2S@MoS_2 nanoboxes to activate H_2O_2 for efficient sulfadiazine degradation? *Chemical engineering journal* **2022**.

29. Zhang, H., ChanZeng, HanxuanWu, HuiyingYang, LingfangDeng, LinShi, Zhou. ZIF-8 assisted synthesis of magnetic core-shell Fe_3O_4@CuS nanoparticles for efficient sulfadiazine degradation via H_2O_2 activation: Performance and mechanism. *Journal of Colloid and Interface Science* **2021**, *594*.
30. Zhang, H.; Zhou, C.; Zeng, H.; Deng, L.; Shi, Z. Can Cu_2ZnSnS_4 nanoparticles be used as heterogeneous catalysts for sulfadiazine degradation? *Journal of Hazardous Materials* **2020**, *395*, 122613, doi:https://doi.org/10.1016/j.jhazmat.2020.122613.
31. Wójcik, S.; Grzybek, G.; Stelmachowski, P.; Sojka, Z.; Kotarba, A. Bulk, Surface and Interface Promotion of Co3O4 for the Low-Temperature N2O Decomposition Catalysis. *Catalysts* **2020**, *10*, 41.
32. Cho, H.; Joo, H.; Kim, H.; Kim, J.-E.; Kang, K.-S.; Jung, H.; Yoon, J. Enhanced Photoelectrochemical Activity of TiO2 Nanotubes Decorated with Lanthanide Ions for Hydrogen Production. *Catalysts* **2022**, *12*, 866.
33. Zhang, L.; Huo, F.; Wang, A.; Chai, S.; Guan, J.; Fan, G.; Yang, W.; Ma, G.; Han, N.; Chen, Y. Coordination-Controlled Catalytic Activity of Cobalt Oxides for Ozone Decomposition. *Inorganic Chemistry* **2023**, *62*, 9178-9189, doi:10.1021/acs.inorgchem.3c01064.
34. Li, W.; Gibbs, G.V.; Oyama, S.T. Mechanism of Ozone Decomposition on a Manganese Oxide Catalyst. 1. In Situ Raman Spectroscopy and Ab Initio Molecular Orbital Calculations. *Journal of the American Chemical Society* **1998**, *120*, 9041-9046, doi:10.1021/ja981441+.
35. Li, X.; Ma, J.; Zhang, C.; Zhang, R.; He, H. Detrimental role of residual surface acid ions on ozone decomposition over Ce-modified γ-MnO2 under humid conditions. *Journal of Environmental Sciences* **2020**, *91*, 43-53, doi:https://doi.org/10.1016/j.jes.2019.12.004.
36. Pietrogiacomi, D.; Sannino, D.; Magliano, A.; Ciambelli, P.; Tuti, S.; Indovina, V. The catalytic activity of CuSO4/ZrO2 for the selective catalytic reduction of NOx with NH3 in the presence of excess O2. **2002**, *36*, 217-230.
37. Yang, S.; Chen, S.; Mosconi, E.; Fang, Y.; Xiao, X.; Wang, C.; Zhou, Y.; Yu, Z.; Zhao, J.; Gao, Y.; et al. Stabilizing halide perovskite surfaces for solar cell operation with wide-bandgap lead oxysalts. *Science* **2019**, *365*, 473-478, doi:doi:10.1126/science.aax3294.
38. Wahlqvist, M.; Shchukarev, A. XPS spectra and electronic structure of Group IA sulfates. *Journal of Electron Spectroscopy and Related Phenomena* **2007**, *156-158*, 310-314, doi:https://doi.org/10.1016/j.elspec.2006.11.032.
39. Smirnov, M.Y.; Kalinkin, A.V.; Pashis, A.V.; Sorokin, A.M.; Noskov, A.S.; Kharas, K.C.; Bukhtiyarov, V.I. Interaction of Al2O3 and CeO2 Surfaces with SO2 and SO2 + O2 Studied by X-ray Photoelectron Spectroscopy. *The Journal of Physical Chemistry B* **2005**, *109*, 11712-11719, doi:10.1021/jp0508249.
40. Ma, G.; Tang, W.; Wang, A.; Zhang, L.; Guan, J.; Han, N.; Chen, Y. Heterojunctioned CuO/Cu2O catalyst for highly efficient ozone removal. *Journal of Environmental Sciences* **2023**, *125*, 340-348, doi:https://doi.org/10.1016/j.jes.2022.01.032.
41. Huang, H.; Li, F.; Wang, H.; Zheng, X. The size controlled synthesis of Cu2S/P25 hetero junction solar-energy-materials and their applications in photocatalytic degradation of dyes. *RSC Advances* **2017**, *7*, 50056-50063, doi:10.1039/C7RA07253H.
42. Fu, S.-Y.; Chang, H.-H.; Hsu, Y.-K.; Lin, Y.-G. Facile synthesis of Cu2S nanoarchitectures in application of surface enhanced Raman scattering. In Proceedings of the Nanophotonic Materials XI, 2014; pp. 25-28.
43. Mai, H.E.; Fang, P.; Xie, G.Q.; Xie, Y.L.; Luo, M.F. Characterization of CuO Species in CuO/CeO_2-Al_2O_3 Catalysts by In-situ XRD, Raman Spectroscopy and TPR. *Acta Physico-chimica Sinica* **2005**, *21*, 997-1000.